# X-ray Study of Residual Stress Distribution of Ground Ceramics*

Yoshihisa SAKAIDA**, Keisuke TANAKA***,
Yuichi IKUHARA**** and Kenji SUZUKI*****

The residual stress distribution of ground ceramics was determined from the eigen strain distributed near the ground surface. The eigen strain of ground ceramics was tensile, and exponentially decreased with the distance from the surface. The residual stress distribution is given as a superposition of an exponential function of compression and a linear function. It is found that the actual residual stress distribution can be approximated by an exponential function of compression because the magnitude of tensile residual stress is negligibly small compared to the compressive residual stress. In the experiments, the diffraction angle was measured on ground silicon nitride for a wide range of $\sin^2\psi$ using the glancing incidence X-ray diffraction technique. A strong nonlinearity was found in the $2\theta$-$\sin^2\psi$ diagram at very high $\psi$-angles. From the analysis of nonlinearity, the residual stress distribution was determined. The residual stress distribution of silicon nitride coincided with the distribution calculated from the eigen strain distribution. Transmission electron microscopy was used to clarify the origin of generation of the residual stress. Both strain contrasts and microcracks were observed below the ground surface; straight dislocations were also observed within silicon nitride grains near the ground surface.

***Key Words***: Ceramics, Residual Stress, Grinding, X-ray Stress Measurement, Dislocation, Glancing Incidence X-ray Diffraction Method, Transmission Electron Microscopy

## 1. Introduction

In order to achieve a precise dimensional tolerance, most of the ceramic components are usually finished by grinding. The grinding process induces residual stresses and grinding flaws on the ground surface, and the fracture strength of ground ceramics greatly depends on these two factors[(1)-(3)]. In the case of compressive residual stresses existing near the component surface, the bending strength and fatigue life is controlled by the surface flaw size relative to the residual stress distribution[(2)]. The exact determination of the grinding residual stress distribution, therefore, is very important to improve the fracture strength of ceramics.

The grinding residual stress distribution has been approximated by the residual stress field beneath the indenter trace such as a Vickers indenter and a hard spherical indenter[(4)-(7)]. In the case of indentation, compressive residual stresses are built up in the close vicinity of the indented surface, while large tensile residual stresses are also introduced right below the compressive residual stress zone. In this case, the fracture strength of ground ceramics is remarkably reduced when the tip of the grinding flaw reaches down to the tensile residual stress field. However, the bending strength in the direction parallel to the grinding direction was found to be larger than the bending strength of specimens without grinding[(2),(3)]. The experimental result is inconsistent with the assumption of a large tensile residual stress below the compressive residual stress zone.

In the present study, the residual stress distribution of ground ceramics was first theoretically

* Received 9th February, 1998. Japanese original: Trans. Jpn. Soc. Mech. Eng., Vol. 63, No. 612, A (1997), p. 1681-1687 (Recieved 22nd November, 1996)
** Research and Development Laboratory, Japan Fine Ceramics Center, 2-4-1 Mutsuno, Atsuta-ku, Nagoya 456-8587, Japan
*** Faculty of Engineering, Nagoya University, Furo-cho, Chikusa-ku, Nagoya 464-8603, Japan
**** Faculty of Engineering, The University of Tokyo, Hongo, Bunkyo-ku, Tokyo 113-8656, Japan
***** Faculty of Education, Niigata University, 8050 Ikarashi-2-no-cho, Niigata 950-2181, Japan



NII-Electronic Library Service

calculated from the tensile eigen strain distributed near the ground surface[9]. The tensile eigen strain was assumed to decrease exponentially with the distance from the surface, and the residual stress distribution was determined. Next, the residual stress state of ground silicon nitride was measured using the glancing incidence X-ray diffraction technique[10]. The measured residual stress distribution was compared to the theoretical residual stress distribution. Finally, in order to examine the origin of grinding residual stresses, cross-sectional observations near the ground surface were performed with transmission electron microscopy.

## 2. Principle of Analysis

### 2.1 Determination of residual stress distribution of ground ceramics

Residual stresses are introduced in ceramics when a ceramics component is subjected to heat treatment or machining. In the case of grinding with a diamond wheel, large compressive residual stresses were measured in the close vicinity of the ground surface using a conventional X-ray stress measurement[10],[11]. The ground surface layer was gradually removed by mechanical polishing with a diamond slurry, and then the X-ray stress measurement was repeated. As a result, the residual stress state was found to be biaxial. The compressive residual stresses decayed exponentially with the distance from the surface and small tensile residual stresses could be measured below the compression zone[2],[3],[12],[13]. During the grinding process, the material in the surface region is extended relative to the interior material because the diamond wheel comes into contact with the surface. Subsequently the surface region ends up in compression. In this study, a tensile eigen strain is induced near the ground surface of ceramic samples during the grinding process, and then grinding residual stresses are generated by the eigen strain distribution.

Figure 1 shows the ground surface ($xy$-plane) of the ceramic specimen which has a rectangular section. The residual stress distribution will be theoretically calculated in a manner similar to previous study reported by Terasaki et al[14]. In this figure, $k$ is the width and $h$ is the thickness of the specimen. The tensile eigen strain of ground ceramics is assumed to exist in the region of $0 \leq z \leq t$, and exponentially decrease with the distance from the ground surface as follows:

$$g_1(z)=g_{10}\exp(-\gamma z)$$
$$g_2(z)=g_{20}\exp(-\gamma z) \qquad (1)$$

where $g_1(z)$ and $g_2(z)$ are the principal eigen strain distributions, $g_{10}$ and $g_{20}$ are the eigen strains on the ground surface and $\gamma$ is a constant. The directions of

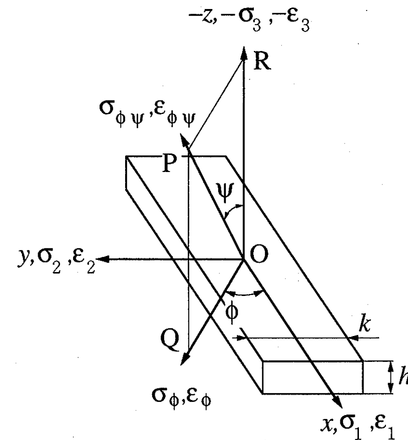


Fig. 1 Definition of coordinate system

$x$-axis and $y$-axis in an orthogonal coordinate system correspond to the directions of the principal strains $\varepsilon_1$ and $\varepsilon_2$.

The strains arisen from elastic response relative to the eigen strains, $g_1(z)$ and $g_2(z)$, parallel to the $x$-axis and $y$-axis are defined as $\varepsilon_x(z)$ and $\varepsilon_y(z)$. The elastic strains are given by

$$\varepsilon_x(z)=a+bz$$
$$\varepsilon_y(z)=a'+b'z \qquad (2)$$

where $a$, $b$, $a'$ and $b'$ are constants. The residual principal stress, $\sigma_1(z)$, in the $x$-direction is obtained as follows:

$$\sigma_1(z)=\frac{E}{1-\nu^2}\{\varepsilon_x(z)-g_1(z)+\nu[\varepsilon_y(z)-g_2(z)]\} \quad (0\leq z\leq t)$$
$$=\frac{E}{1-\nu^2}[\varepsilon_x(z)+\nu\varepsilon_y(z)] \quad (t\leq z\leq h) \qquad (3)$$

Here consider the equations of equilibrium for residual stresses and bending moments. After grinding, the ground specimen is in static equilibrium. The total force acting on the specimen in the $x$-direction must be zero. The equation of equilibrium relating the residual principal stress $\sigma_1(z)$ is

$$\int_0^h \sigma_1(z)dz=0 \qquad (4)$$

The bending moment relative to $y$-axis must be also zero. The equation of equilibrium relating the bending moment is

$$\int_0^h \sigma_1(z)zdz=0 \qquad (5)$$

Similarly, for the principal stress $\sigma_2(z)$, the equations of equilibrium such as Eqs.(4) and (5) must be satisfied. From the above equations, the constant parameters, $a$, $b$, $a'$ and $b'$, are determined mathematically. Substituting the obtained constant parameters into Eq.(3), the residual stress distributions, $\sigma_1(z)$ and $\sigma_2(z)$, can be determined.

For simplicity, the case where $g_2(z)=g_1(z)$ is first considered. The residual stress distributions can



NII-Electronic Library Service

easily be determined as follows. For elastic strains (Eq. (2)), $\varepsilon_y(z)=\varepsilon_x(z)$, because $g_2(z)=g_1(z)$. The constant parameters, $a$ and $b$, are given by

$$a=\frac{2g_{10}}{\gamma h}\left\{\left(\frac{3}{\gamma h}-2\right)[\exp(-\gamma t)-1]+\frac{3t}{h}\exp(-\gamma t)\right\}$$
$$b=-\frac{6g_{10}}{\gamma h^2}\left\{\left(\frac{2}{\gamma h}-1\right)[\exp(-\gamma t)-1]+\frac{2t}{h}\exp(-\gamma t)\right\} \quad (6)$$

Therefore the principal residual stress distributions are expressed as

$$\sigma_1(z)=\sigma_2(z)=\frac{E}{1-\nu}[a+bz-g_{10}\exp(-\gamma z)] \quad (7)$$

It must be noted that the residual stress distribution is represented as a superposition of an exponential function of compression and a linear function. For example, for $h=t=4$ mm, $g_{10}=3.0\times10^{-3}$ and $\gamma=100$ mm$^{-1}$, Eq. (7) becomes

$$\sigma_1(z)=\sigma_2(z)=11.96-4.48z-1200\exp(-100z) \quad (8)$$

where the unit of the residual stress, $\sigma_i(z)$, is megapascal (MPa) and the unit of the distance, $z$, is millimeter (mm). In this study, internal stresses due to eigen strains, $g_i(z)$, are denoted by $\sigma^*$. The internal stress in the ground specimen is expressed as $\sigma^*=-1200\exp(-100z)$.

Figures 2 (a) and (b) show an example of the principal residual stress distribution arisen from the tensile eigen strains distributed near the ground surface. In this figure, the dotted-dashed line indicates the residual stress, $\sigma_i(z)$, drawn in accordance with Eq. (8) and the solid line indicates the compressive internal stress, $\sigma^*$. Near the ground surface, the residual stress nearly coincides with the internal stress as shown in Fig. 2 (a). It should be noted that the residual stress in the close vicinity of the ground surface can be approximated by an exponentially decreasing function with the distance, $z$. Figure 2 (b) shows the distribution of the residual stress, $\sigma_i(z)$, with distance, $z$, throughout the thickness of the ground specimen. The region of tensile residual stresses due to the force balance to the compressive residual stress field near the ground surface extends from 0.05 to 2.66 mm in thickness. Near the back side of the specimen, the residual stress is compressive again. The maximum tensile residual stress is about 11.5 MPa. The magnitude of the tensile residual stress is negligibly small compared to the compressive residual stress; the percentage of the maximum tensile residual stress to the maximum compressive residual stress is about 1.0%. In the case of ceramics with a Vickers indentation, a large tensile residual stress field is expected beneath an indenter trace[8]. On the other hand, for the ground ceramics, the tensile residual stress field is very small. The residual stress due to indentation can not be used for modeling the grinding residual stress distribution.

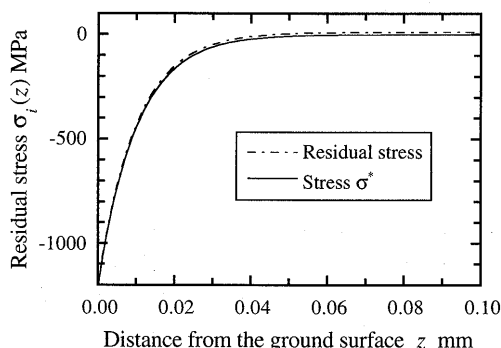


(a) Residual stress below the ground surface

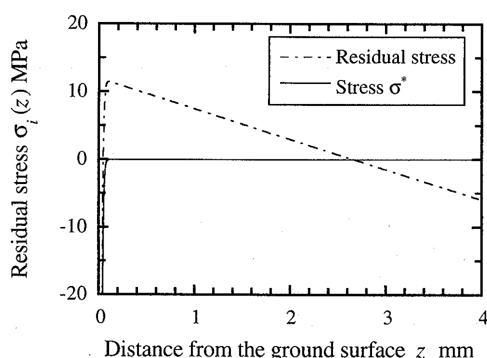


(b) Residual stress distribution from the ground side to the back side

Fig. 2 Residual stress distribution of the ground specimen

From the above theoretical analysis, a large compressive residual stress field induced during the grinding process is concluded to be restricted to the vicinity of the ground surface. Furthermore, the compressive residual stress exponentially decreases with the distance from the ground surface and the tensile residual stress field is widely distributed beneath the compressive residual stress field so as to satisfy the force balance within the specimen thickness.

### 2.2 Estimation of the $2\theta$-$\sin^2\psi$ diagram in X-ray stress measurement

From the previous section, when the ceramic specimen with a finite thickness, $h$, is ground on one side, the grinding residual stress distribution within the specimen is expressed by

$$\sigma_1(z)=a_0+a_1z+\sigma_{10}\exp(-\gamma z) \quad (9)$$

where $\sigma_1(z)$ is a principal residual stress and $a_0$, $a_1$ and $\sigma_{10}$ are constants. The other principal residual stress, $\sigma_2(z)$, is given by

$$\sigma_2(z)=\beta\cdot\sigma_1(z) \quad (10)$$

where $\beta$ is a proportionality constant. The lattice strain $\varepsilon_{\phi\psi}(z)$ in OP direction shown in Fig. 1 is given by



NII-Electronic Library Service

$$\varepsilon_{\phi\psi}(z)=\frac{1+\nu}{E}[\sigma_1(z)\cos^2\phi+\sigma_2(z)\sin^2\phi]\sin^2\psi$$
$$-\frac{\nu}{E}[\sigma_1(z)+\sigma_2(z)] \quad (11)$$

where $E$ is Young's modulus and $\nu$ is Poisson's ratio.

The lattice strain $\langle\varepsilon_{\phi\psi}\rangle$ determined by X-rays can be expressed as the weighted average of the lattice strain $\varepsilon_{\phi\psi}(z)$ as follows[15]:

$$\langle\varepsilon_{\phi\psi}\rangle=\frac{\int_0^\infty \varepsilon_{\phi\psi}(z)\exp(-z/T_0)dz}{\int_0^\infty \exp(-z/T_0)dz} \quad (12)$$

where $T_0$ is the effective X-ray penetration depth. For an $\Omega$ goniometer, $T_0$ is given by

$$T_0=\frac{\sin^2\theta_0-\sin^2\psi}{2\mu\sin\theta_0\cos\psi} \quad (13)$$

where $2\theta_0$ is the diffraction angle from the stress-free material and $\mu$ is the linear absorption coefficient.

The strains $\langle\varepsilon_{\phi\psi}\rangle$ for $\phi=0$ and $\phi=\pi/2$ are denoted by $\langle\varepsilon_{\phi=0}\rangle$ and $\langle\varepsilon_{\phi=\pi/2}\rangle$. These strains are obtained by substituting Eq.(11) into Eq.(12) as follows:

$$\langle\varepsilon_{\phi=0}\rangle=\left[-\frac{\nu(\beta+1)}{E}+\frac{1+\nu}{E}\sin^2\psi\right]$$
$$\times\left(a_0+a_1T_0+\frac{\sigma_{10}}{\gamma T_0+1}\right) \quad (14)$$
$$\langle\varepsilon_{\phi=\pi/2}\rangle=\left[-\frac{\nu(\beta+1)}{E}+\frac{\beta(1+\nu)}{E}\sin^2\psi\right]$$
$$\times\left(a_0+a_1T_0+\frac{\sigma_{10}}{\gamma T_0+1}\right) \quad (15)$$

The diffraction angle for diffractions from lattice planes with the normal parallel to OP direction is denoted by $\langle 2\theta_{\phi\psi}\rangle$. The lattice strain, $\langle\varepsilon_{\phi\psi}\rangle$, is determined from the change of the diffraction angle as

$$\langle 2\theta_{\phi\psi}\rangle=2\theta_0-2\tan\theta_0\cdot\langle\varepsilon_{\phi\psi}\rangle \quad (16)$$

The diffraction angle $\langle 2\theta_{\phi\psi}\rangle$ for $\phi=0$ and $\phi=\pi/2$ are denoted by $\langle 2\theta_{\phi=0}\rangle$ and $\langle 2\theta_{\phi=\pi/2}\rangle$. From the above equation, the relation between the diffraction angles, $\langle 2\theta_{\phi=0}\rangle$ and $\langle 2\theta_{\phi=\pi/2}\rangle$, and $\sin^2\psi$ can be obtained by substituting Eqs.(14) and (15) into Eq.(16).

Figure 3 shows the $2\theta$-$\sin^2\psi$ diagram for the residual stress distribution described by Eq.(8). In this calculation, the diffraction from $Si_3N_4$ 212 plane by Cr-K$\alpha$ radiation was used. In this figure, the dotted line indicates the result when the first and second terms of the right side in Eq.(8) are neglected. The diffraction angle in both cases increases with an increase in $\sin^2\psi$. The $2\theta$-$\sin^2\psi$ diagrams show a concave curvature. It is noteworthy that the influence of the first and second terms in Eq.(8) on the $2\theta$-$\sin^2\psi$ diagram is very small, because the solid line almost coincides with the dotted line. Therefore the actual grinding residual stress distribution estimated by X-ray stress measurement can be approximated by the compressive exponential function as follows:

$$\sigma_1(z)=\sigma_{10}\exp(-\gamma z)$$
$$\sigma_2(z)=\beta\cdot\sigma_1(z) \quad (17)$$

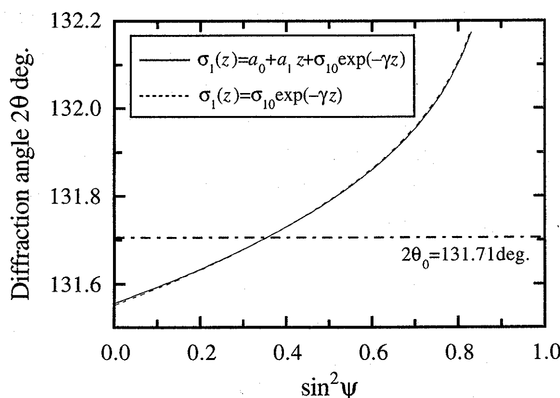


Fig. 3 $2\theta$-$\sin^2\psi$ diagram predicted from an exponential residual stress distribution

## 3. Experimental Procedure

### 3.1 Material and specimen

The material used in this study was pressureless sintered silicon nitride, designated as SN73M (manufactured by NGK Insulators, Ltd. in Japan). The compositions and mechanical properties of silicon nitride are summarized in Table 1. The surface of specimen was ground parallel to the longitudinal $x$-direction by the surface grinding method. The grit size of the diamond wheel was #200/230. The grinding conditions were summarized in Table 2.

### 3.2 X-ray stress measurement using the glancing incidence X-ray diffraction technique

The grinding residual stress distribution was measured using the glancing incidence X-ray diffraction technique (GIXD). An X-ray stress measurement using GIXD technique is a new method which is applicable to the estimation of the residual stress field having steep stress gradients within the effective penetration depth $T_0$[10]. Figure 4 shows the geometry of the GIXD method. In the conventional

Table 1 Properties of material

| Composition (wt%) | $Si_3N_4$ | Mg | Ce | Sr | T-O |
|---|---|---|---|---|---|
| | 89 | 2.0 | 3.5 | 0.7 | 4.8 |
| Density ρ (kg/m³) | | | | 3.23×10³ | |
| 4-point bending strength $\sigma_B$ (MPa) | | | | 945 | |
| Fracture toughness $K_{IC}$*1 (MPa√m) | | | | 6.6 | |
| Young's modulus $E$*2 (GPa) | | | | 288 | |
| Poisson's ratio ν*2 | | | | 0.28 | |

*1) $K_{IC}$ was measured by SEPB method.
*2) Stiffness was measured by pulse echomethod.

Table 2 Surface grinding conditions

| Grinding method | Plunge surface grinding, Up-cut |
|---|---|
| Grinding wheel | SDC200/230N75B<br>Size: $350^D\times20^T\times127^H$ mm (14A1) |
| Peripheral wheel speed $V_S$ (m/min) | 2000 |
| Workpiece speed $V_W$ (m/min) | 10 |
| Depth of cut Δ (μm/pass) | 6 |



NII-Electronic Library Service

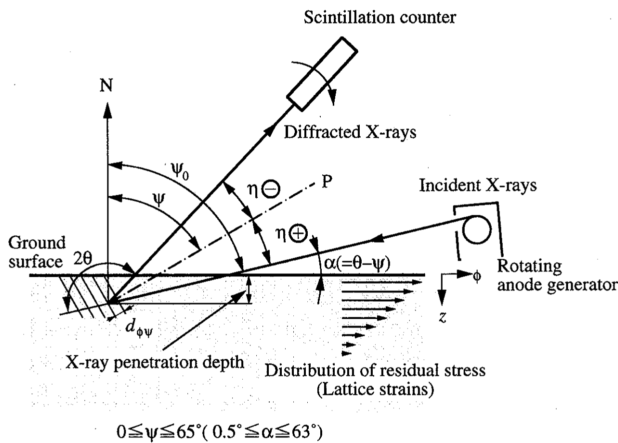


Fig. 4 X-ray stress measurement using a glancing incidence X-ray diffraction technique

Table 3 X-ray conditions for stress measurement

| Measurement principle | Ω-goniometer Fixed $\psi_0$ (−η) |
|---|---|
| Characteristic X-ray | Cr-Kα |
| Tube voltage (kV) | 50 |
| Tube current (mA) | 100 |
| Divergent slit (mm²) | 0.4 × 5 |
| Step angle (deg.) | 0.02 |
| Fixed time (sec.) | 1~20 |
| Diffraction | 212 of β-$Si_3N_4$ |
| Diffraction angle $2\theta_0$ (deg.) | 131.71 |
| Incident angle α (deg.) | 0.5, 1.0, 2.0, 3.0, 4.0, 7.0, 10, 13, 16, 19, 21, 24, 27, 30, 33, 36, 40, 43, 48, 53, 63 |

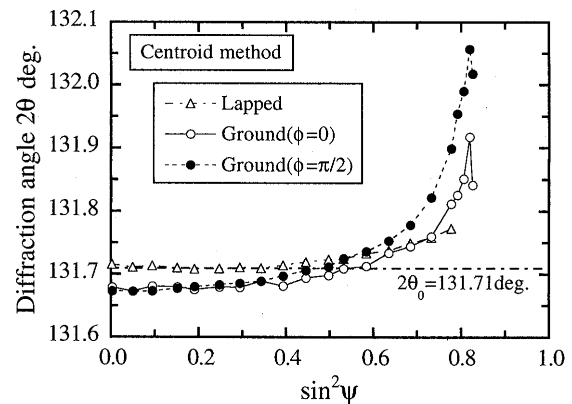


Fig. 5 $2\theta$-$\sin^2\psi$ diagram for 212 diffraction by Cr-K$\alpha$ radiation

$\sin^2\psi$ method, X-rays are irradiated from the $-\eta$ side and the detector is located on the $+\eta$ side, where $\eta=\pi/2-\theta$. In the present study, to measure the lattice strains for a wide range of $\psi$ for the Ω-goniometer, a scintillation counter is located on the $-\eta$ side and an incident X-ray beam impinges on the ground surface from the $+\eta$ side. In the GIXD method, the $\psi$-angle is given by

$$\psi=\theta-\alpha \quad (18)$$

where $\alpha$ is the X-ray incident angle[10],[16]. The incident angle ranges from 0.5 to 63 degrees. The diffraction angle of $Si_3N_4$ 212 diffraction by Cr-K$\alpha$ radiation was measured for several $\psi$-tilts in the $x$-direction ($\phi=0$) and in the $y$-direction ($\phi=\pi/2$). The lapped specimen was also prepared to obtain the diffraction angle from the stress free silicon nitride. The $2\theta$-$\sin^2\psi$ diagram for both the ground specimen and the lapped specimen was measured. In the experiment, the peak position was determined by the centroid method. Table 3 summarizes the X-ray conditions for stress measurement. The linear absorption coefficient of the material was $\mu=317\ \mathrm{cm}^{-1}$.

## 4. Experimental Results and Discussion

### 4.1 $2\theta$-$\sin^2\psi$ diagram for ground ceramics measured by GIXD method

Figure 5 shows $2\theta$-$\sin^2\psi$ diagrams of ground and lapped specimens. For the ground specimen, the diffraction angle increases monotonously with an increase in $\sin^2\psi$, and rises drastically at about 0.7 of $\sin^2\psi$. A strong nonlinearity is found in the $2\theta$-$\sin^2\psi$ diagram especially at very high $\psi$-angles. The diffraction angle at $\sin^2\psi=0.83$ is slightly smaller than the maximum diffraction angle. At $\sin^2\psi=0.83$, the X-ray incident angle, $\alpha$, is equal to 0.5 deg.; the incident X-ray beam nearly horizontally impinges on the ground surface. Since the grinding residual stress was relaxed on the surface, the weighted average angle $\langle 2\theta_{\phi\psi}\rangle$ at the close vicinity of the ground surface becomes slightly small. The change of the diffraction angle for $\phi=\pi/2$ is larger than that for $\phi=0$. It suggests that the principal stress, $\sigma_2(z)$, perpendicular to the grinding direction is larger than the other principal stress, $\sigma_1(z)$, parallel to the grinding direction. A similar nonlinearity in the $2\theta$-$\sin^2\psi$ diagram of ground $Si_3N_4$ was reported by Eigenmann et al.[11] They measured $2\theta$-$\sin^2\psi$ diagrams of $Al_2O_3$, $Al_2O_3$/TiC and $Y_2O_3$-stabilized $Zr_2O_3$ using a $\Psi$-goniometer.

On the other hand, for the lapped specimen, the diffraction angle is nearly constant up to $\sin^2\psi=0.5$. Above $\sin^2\psi=0.5$, the diffraction angle increases slightly. Since the residual stress distribution of the lapped specimen is similar to the distribution of the ground specimen[17], a slight increment in the diffraction angle at high $\psi$-angles takes place. However, the maximum compressive residual stress of the lapped specimen is considerably smaller than that of the ground specimen and the depth of the compressive residual stress field is shallower. The weighted average angle at low $\psi$-angles, where the effective penetration depth is relatively deep, is nearly equal to the diffraction angle, $2\theta_0$, from the stress free silicon nitride. In this study, the average diffraction angle over the $\sin^2\psi$ range from zero to 0.5 is used for the



NII-Electronic Library Service

stress-free diffraction angle. Thus $2\theta_0=131.71°$.

## 4.2 Determination of grinding residual stress distribution

The $2\theta$-$\sin^2\psi$ relation was derived by substituting Eqs. (14) and (15) into Eq. (16) under the assumption of $a_0=a_1=0$. By fitting the derived $2\theta$-$\sin^2\psi$ relation to the experimental data, as shown in Fig. 5, the residual stress distribution is determined from optimizing the parameters $\gamma$, $\sigma_{10}$, $\beta$ and $2\theta_0$ by a least-square method. Figure 6 shows the estimated residual stress distributions, $\sigma_1(z)$ and $\sigma_2(z)$. The principal residual stress $\sigma_2(z)$ in $y$-direction ($\phi=\pi/2$) is larger than the principal stress $\sigma_1(z)$ in $x$-direction ($\phi=0$), and then $\beta=1.35$. To confirm the validity of the residual stress distributions shown in Fig. 6, the $2\theta$-$\sin^2\psi$ relation was calculated from the estimated residual stress distributions of $\sigma_1(z)$ and $\sigma_2(z)$. Figure 7 shows the calculated $2\theta$-$\sin^2\psi$ diagram, compared with the experimental data. In this figure, the dotted-dashed line indicates the optimum stress-free diffraction angle $2\theta_0$. The each calculated curve fits well to the experimental data. Furthermore, the optimum stress-free diffraction angle coincides with the experimental data determined from the lapped specimen. It can be concluded that the grinding residual stress distribution can be approximated by Eq. (17).

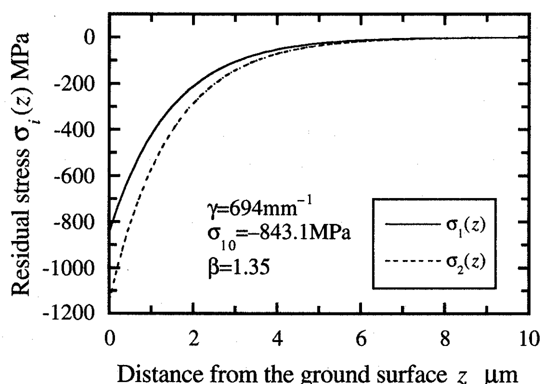


Fig. 6 Residual stress distribution of ground $Si_3N_4$

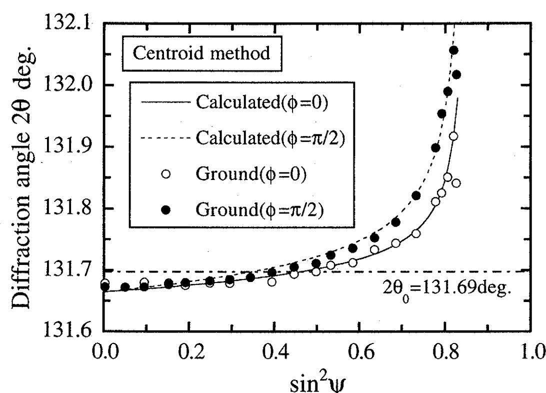


Fig. 7 $2\theta$-$\sin^2\psi$ diagram calculated from the estimated stress distribution

## 4.3 Microscopic observation near the ground surface using transmission electron microscopy

Figure 8 shows the relation between the full width at the half maximum intensity of diffraction profiles (FWHM), $B$, and $\sin^2\psi$ for the ground and lapped specimens. For the ground specimen, the breadth for $\phi=0$ and $\phi=\pi/2$ is wider than the breadth of the lapped specimen. A drastic increase in the breadth takes place in the $\sin^2\psi$ range from 0.7 to 0.83. A similar tendency is seen in the $2\theta$-$\sin^2\psi$ diagram. The magnitude of the breadth changes depending on the amount of plastic deformation or nonuniform strains within the material; the breadth becomes wider, as the amount of plastic deformation and nonuniform strain get larger. The increment of the breadth for $\sin^2\psi\geq0.7$ suggests that plastic deformation is generated in the close vicinity of the ground surface, because the effective X-ray penetration depth decreases with an increase in $\sin^2\psi$.

In this study, to clarify an origin of the generation of residual stresses, the cross-sectional observations were performed with transmission electron microscopy (JEM 4000FX, JEOL). The existence of plastic deformation or dislocations was examined near the ground surface. In order to observe dislocations from the cross-sectional view, the thickness of the specimen must be enough thin. However, most of the thin specimen broke by the remaining grinding flaws such as median cracks when the ceramics specimen ground by the surface grinding method was thinned. The cross-sectional TEM specimen was prepared as follows: The surface of silicon nitride specimen was ground by the face grinding method where the grinding flaws are hardly left on the ground surface[(3)]. After grinding, two cut pieces were glued together by the epoxy with the ground surface facing each other. Sandwiched specimens were thinned by polishing to

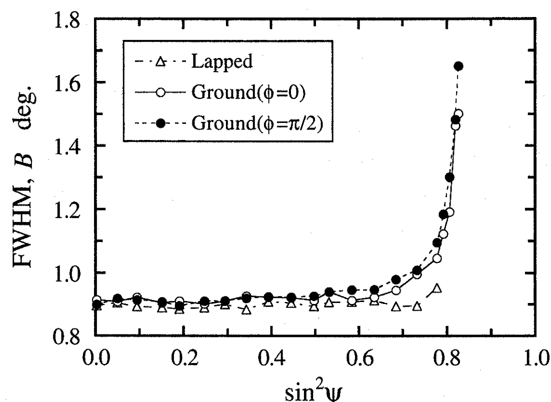


Fig. 8 Relation between FWHM and $\sin^2\psi$ for 212 diffraction by Cr-K$\alpha$ radiation



NII-Electronic Library Service

Table 4 Face grinding conditions

| | |
|---|---|
| Grinding method | Face grinding |
| Grinding wheel | SDC400/500N75B<br>Size: $100^D \times 3^W \times 3^X \times 31.75^H$ mm (6A2) |
| Peripheral wheel speed $V_S$ (m/min) | 1500 |
| Feed rate $V_F$ (m/min) | 500 |
| Depth of cut $\Delta$ (μm/pass) | 5 |

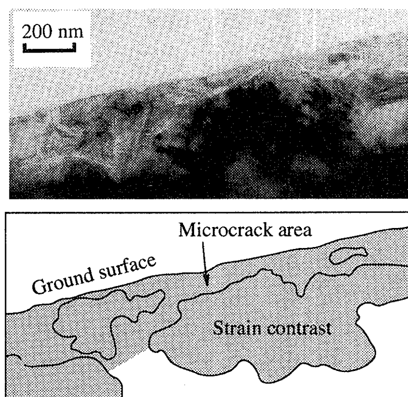


(a) Strain contrasts and microcracks observed below the ground surface

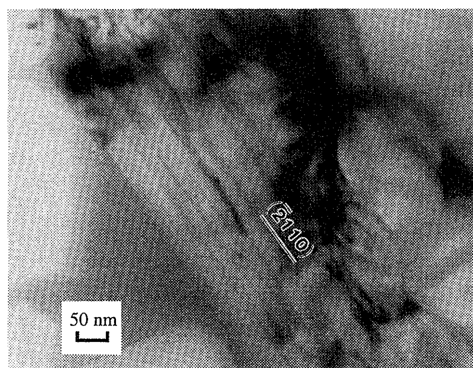


(b) Dislocation located within silicon nitride grains. The incident beam direction is parallel to [1 2 $\bar{3}$ $\bar{1}$]

Fig. 9 Cross-sectional bright-field image obtained from the face-ground $Si_3N_4$ using transmission electron microscopy

the thickness of about 0.1 mm. After attaching them to Mo rings for reinforcement, the center of the region facing each other was dimpled to the thickness of 20 $\mu$m, and further thinned by ion beam sputtering. Table 4 summarizes the face grinding conditions.

Figure 9 shows an example of the bright-field micrograph obtained from the face-ground specimen. The upper face in this figure corresponds to the ground surface. The region between the ground surface and the depth of 200 nm was observed from a cross-sectional view. Both strain contrasts due to residual strains and microcracks were observed below the ground surface as illustrated in Fig. 9(a). Figure 9(b) shows a magnified bright-field image of the strain contrast region. Straight dislocations in the direction parallel to $\bar{2}$110 plane were also observed within silicon nitride grains near the ground surface, as black lines seen in Fig. 9(b). It is suggested that several grains located near the ground surface were deformed plastically. Any dislocation usually cannot be observed in any grain of silicon nitride after pressureless-sintering. Dislocations seen on the silicon nitride creep-deformed at elevated temperature are not straight(18). It can be concluded that straight dislocations seen in this study are a characteristic feature of dislocations generated on ground ceramics.

From the analysis of the grinding residual stress distribution of ceramics, ceramics are plastically deformed by a diamond wheel and a compressive residual stress is generated near the ground surface. Furthermore, the grinding residual stress for ceramics can be approximated as an exponential decrement with an increase in depth from the ground surface.

## 5. Conclusion

The residual stress distribution of ground ceramics was theoretically examined, and was compared to the experimental data obtained from the surface-ground silicon nitride. In order to examine plastic deformations, cross-sectional observations near the ground surface were performed with transmission electron microscopy. The results are summarized as follows:

(1) The residual stress distribution was determined in the case where the tensile eigen strain is distributed near the ground surface and exponentially decreases with the distance from the surface. The residual stress distribution can be expressed as a superposition of an exponential function and a linear function. In the case of ground ceramics, a tensile residual stress field is not large such as indented ceramics, but a small stress field where force balance is satisfied over the thickness of specimens. The balancing tensile stress field is widely distributed beneath the compressive residual stress field, and is negligibly small.

(2) The $2\theta$-$\sin^2\psi$ relation was measured either parallel or perpendicular to the grinding direction using the glancing incidence X-ray diffraction technique. The experimental data agrees well with the theoretical $2\theta$-$\sin^2\psi$ relation based on the assumption that the residual stress distribution is expressed as an exponential function.

(3) Straight dislocations were observed within silicon nitride grains near the ground surface. Several grains located near the ground surface were plastically deformed, and give rise to the generation of residual stresses. Both strain contrasts due to residual



NII-Electronic Library Service

strains and microcracks were also observed below the ground surface.

**Acknowledgments**

This research sponsorship by AIST, MITI, Japan, as a part of the Synergy Ceramics Project of ISTF program is greatly appreciated.

**References**

(1) Samuel, R., Chandrasekar, S., Farris, T.N. and Licht, R.H., J. Am. Ceram. Soc., Vol. 72, No. 10 (1989), p. 1960-1966.
(2) Sakaida, Y., Tanaka, K., Suzuki, K. and Kawamoto, H., J. Soc. Mater. Sci. Jpn., (in Japanese), Vol. 44, No. 504 (1995), p. 1127-1132.
(3) Sakaida, Y., Tanaka, K. and Tanaka, S., J. Soc. Mater. Sci. Jpn., (in Japanese), Vol. 45, No. 7 (1996), p. 752-758.
(4) Marshall, D.B., Evans, A.G., Khuri-Yakub, B.T., Tien, J.W. and Kino, G.S., Proc. R. Soc. London., Vol. A385 (1983), p. 461-475.
(5) Tanaka, Y. and Park, G.H., J. Soc. Mater. Sci. Jpn., (in Japanese), Vol. 41, No. 461 (1992), p. 260-266.
(6) Murata, K., Mizutani, K. and Tanaka, Y., J. Soc. Mater. Sci. Jpn., (in Japanese), Vol. 41, No. 464 (1992), p. 624-630.
(7) Murata, K., Mizutani, K. and Tanaka, Y., J. Soc. Mater. Sci. Jpn., (in Japanese), Vol. 43, No. 490 (1994), p. 772-778.
(8) Lawn, B.R. and Swain, M.V., J. Mater, Sci., Vol. 10 (1975), p. 113-122.
(9) Mura, T. and Mori, T., Micromechanics, (1976), 1, Baifu-kan.
(10) Sakaida, Y., Harada, S. and Tanaka, K., J. Soc. Mater. Sci. Jpn., (in Japanese), Vol. 42, No. 477 (1993), p. 641-647.
(11) Eigenmann, B. and Macherauch, E., Z. Metallkd., Vol. 86, No. 2 (1995), p. 84-90.
(12) Kishimoto, H., Ueno, A., Kawamoto, H. and Kondo, S., J. Soc. Mater. Sci. Jpn., (in Japanese), Vol. 36, No. 407 (1987), p. 810-816.
(13) Suzuki, K. and Tanaka, K., J. Soc. Mater. Sci. Jpn., (in Japanese), Vol. 40, No. 454 (1991), p. 818-824.
(14) Terasaki, T., Akiyama, T. and Yoshimura, N., Trans. Jpn. Soc. Mech. Eng., (in Japanese), Vol. 59, No. 567, A (1993), p. 2694-2701.
(15) Suzuki, K., Tanaka, K. and Sakaida, Y., J. Soc. Mater. Sci. Jpn., (in Japanese), Vol. 45, No. 7 (1996), p. 759-765.
(16) Predecki, P., Zhu, X. and Ballard, B., Advances in X-ray Analysis, Vol. 36 (1993), p. 237-245.
(17) Saito, T., Doke, Y., Sakaida, Y. and Ikuhara, Y., Jpn. J. Appl. Phys., Vol. 34, No. 6A (1995), p. 3198-3203.
(18) Kawahara, K., Tsurekawa, S. and Nakashima, H., J. Jpn. Inst. Met., (in Japanese), Vol. 60, No. 6 (1996), p. 582-588.



NII-Electronic Library Service